Fragmentation instabilities of a drop as it falls in a miscible fluid[a]

S. Residori[1], P.K. Buah-Bassuah[2], and F.T. Arecchi[3]

[1] Institut Non-Linéaire de Nice, 1361 route des Lucioles, 06560 Valbonne, France
[2] Physics Department of the University of Cape Coast, Cape Coast, Ghana
[3] Physics Department, University of Florence, Largo E. Fermi 6, 50125 Florence, Italy

Abstract. We review here a series of experiments on the fragmentation instabilities that a liquid drop undergoes as it falls inside a fluid with which it is miscible, so called the solvent. Motivated by the original experiments initiated by Thomson and Newall in 1885, we started to investigate this subject more than one decade ago, encountering up to date a number of challenging problems in hydrodynamical instabilities, complicated by the presence of transient interfaces between the drop and the solvent. In particular, we have shown that when a drop of liquid is deposited over the surface of the same liquid, it falls down inside the solvent because the energy associated to its surface tension against air is instantaneously converted into kinetic energy. As a consequence, a very fast fluid injection takes place as the drop touches the free surface of the solvent and the drop enters inside the solvent. Due to the hydrodynamical instabilities related to the large velocity gradients, it develops into a ring that expands radially. The ring continues to go downwards inside the solvent until it stops at a certain height due to viscous dissipation. In the first stages of the ring expansion, a fluid membrane remains attached to the ring, so-called "turban" for its shape, which is concave or convex depending on the sign of the density difference between the drop and the solvent. When a small density difference is introduced between the drop and the solvent, the ring becomes unstable because of density gradients and it fragments into smaller droplets. On their turn, the secondary droplets may undergo the same instability and may fragment again, so that a cascade of fragmentation takes place. If the density difference is positive, that is, the drop is heavier than the solvent, the secondary droplets continue to go down deeper inside the solvent, until the whole process is washed out by the slow diffusion of the concentration gradients. When the density difference between the drop and the solvent is negative, then the secondary droplets rise up to the free surface of the solvent, where they are distorted by the equivalent of an impact with a rigid wall. Universal scaling laws for the cascade of fragmentation and for the dynamical behavior of the drop have been derived and accompany the experimental observations.

1 Introduction

More than a century after the first report by J.J. Thomson and H.F. Newall [1], the problems related to the hydrodynamical instabilities of a drop falling in a miscible fluid are still challenging and have been recently reconsidered. A section devoted to this phenomenon can be found, for

---

example, in the book of D'Arcy W. Thomson [2]. The complexity of the hydrodynamic process arises from the simultaneous presence of two hydrodynamic instabilities, Kelvin-Helmoltz (KH) and Rayleigh-Taylor (RT), coming from the presence of velocity and density gradients between the drop and the solvent. Moreover, the hydrodynamical problem is complicated by the presence of a transient interfaces between the drop and the solvent and the question arises about the existence of dynamical interface which would appear between two miscible fluids. For instance, the fact that the process of break-up is not, in general, observed for immiscible fluids still has no clear explanation. Actually, a break-up into two fragments has been recently observed in one experiment with two immiscible fluids [3], but this observation requires the drop being loaded with some surfactant and travelling such a long distance as 2 m. It is clear that surface tension plays some important role and that, even in the case of miscible fluids, it is reasonable to ask whether or not we should consider some sort of transient surface tension [4].

In the case of zero density difference between the drop and the solvent, that is the two are made of the same fluid, we have shown that when the drop is deposited over the free surface of the same liquid, it falls down inside the solvent because the energy associated to its surface tension against air is instantaneously converted into kinetic energy [5]. As a consequence, a very fast fluid injection takes place as the drop touches the free surface of the solvent and enters inside the solvent. Due to the hydrodynamical instabilities related to the large velocity gradients, it develops into a ring that expands radially. The ring continues to go downwards inside the solvent until it stops at a certain height due to viscous dissipation. In the first stages of the ring expansion, a fluid membrane remains attached to the ring, so-called "turban" for its shape, which is concave or convex depending on the sign of the density difference $\Delta\rho$ between the drop and the solvent. When $\Delta\rho$ is introduced, the ring becomes unstable because of density gradients and it fragments into smaller droplets. On their turn, the secondary droplets may undergo the same instability and may fragment again, so that a cascade of fragmentations takes place. If the density difference is positive, that is, the drop is heavier than the solvent, the secondary droplets continue to go down deeper inside the solvent, until the whole process is washed out by the slow diffusion of the concentration gradients. We have shown that the fragmentation process is ruled by two non dimensional numbers, the fragmentation number F and the Schmidt number S [6,7] and displays fractal properties in the statistics of the drop fragments [8]. When the density difference between the drop and the solvent is negative (the drop is lighter than the solvent), then the secondary droplets rise up to the free surface of the solvent [9], where they are distorted by the equivalent of an impact with a rigid wall. Universal scaling laws for the cascade of fragmentation and for the dynamical behavior of the drop have been derived and accompany the experimental observations.

The paper is organized as follows. Section 2 presents the experimental setup. Section 3 is dedicated to the first stages of the drop evolution, with its transformation into a torus and the associated scaling laws. The case of a positive density difference between the drop and the solvent is discussed in section 4, where the non-dimensional numbers ruling the fragmentation cascade are introduced. In section 5, the fractal properties of the fragmentation instability are presented. Finally, section 6 is dedicated to the case of a negative density difference with the inverse cascade of fragments rising up to the free surface of the solvent.

2 Experimental setup

A schematic drawing of the experiment is shown in figure 1. The setup consists of a glass cell with a base of $10 \times 10\,\mathrm{cm}^2$ and 40 cm high, mounted on a rigid metallic support. On the top of the cell it is mounted a calibrated microsyringe that releases the drops. Drop volumes from 0.1 to $50\,\mu\mathrm{l}$ are obtained by using Hamilton microsyringes covering different volume ranges, so that the volume uncertainty is of the order of a few percents for all the volumes used. For each volume range, the syringe needle has an edge with a circular section, the diameter of which is sufficiently large to sustain a pending drop [12], with a corresponding Bond number $Bo = \rho g r^2/\sigma < 1$, where ρ is the density of the drop, r its radius, g the acceleration of gravity and σ the surface tension. Thus, the weight of the drop is balanced by the adhesion of the fluid
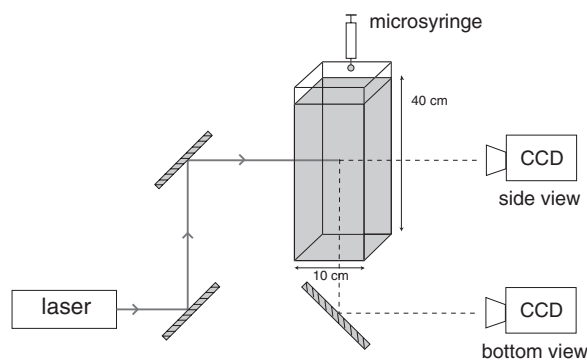
Fig. 1. Experimental setup.

to the needle walls, so that we can consider that gravity is not playing a role in the first stages of the process. Once the drop is formed at the edge of the needle, by means of a micrometric translation stage, we deposit it with adiabatically zero velocity on the free surface of the solvent. The drop is doped with a small amount of sodium fluorescein dye (10^{-8} mol/l) and is visualized by illuminating the cell with a collimated and expanded argon laser beam. Two CCD cameras are used to register the drop, one camera recording the sideview and the other one recording, from the bottom of the cell, the transverse section. The amount of fluorescein dye is sufficiently low in order not to alter the fluid properties and the dimensions of the cell are large enough in order not to influence the drop dynamics [13].

3 The drop injection and the ring formation

To study the early stages of the drop instability, we have focused on the case $\Delta\rho = 0$, that is, the drop and the solvent are made of the same fluid [5]. In such a case, there is no fragmentation since this is ruled by the Rayleigh-Taylor instability arising from the density difference between the drop and the surrounding fluid. The remaining mechanism for the drop instability is of Kelvin-Helmoltz type, that is, the whole process is ruled by velocity gradients. Indeed, when the drop enters inside the solvent, it acquires a high initial speed from the instantaneous conversion of surface energy into kinetic energy. Because of the fast injection and velocity gradients, the fluid jet enrolls onto itself giving rise to a vortex ring. The rotational motion of the fluid induces a transverse component of velocity and the ring expands horizontally while travelling downwards. Thus, the drop transforms from a spherical into a toroidal shape. In figure 2 we show a few lateral images of a water drop entering inside water. The process of injection is very fast and the CCD repetition rate (40 ms) does not permit to follow it. In order to catch the essential features of the process, we set the integration time of the CCD to the minimum available for our system, that is $50\,\mu$s, and we record images for different events of the drop injection, the initial time of each record being different and hazardous at each shot. Then, we extract from the collection of images four successive stages that we show in figure 2. We can see that the injection gives rise to a rapid jet incoming from the point of contact between the drop and the solvent. The drop fluid enters the solvent through the jet and rolls up into a vortex ring. Two-dimensional experiments performed in a Hele-Shaw geometry have also revealed the vortical fluid motion taking place inside the drop during the first stages of evolution [14].

When the kinetic energy is completely dissipated by viscous processes, the ring stops and starts to fade away because of diffusion. We can use a simple dimensional argument to predict the height h at which the ring will stop. By balancing the surface energy $4\pi\sigma r^2$ and the kinetic energy $4/3\pi r^3 \rho v_0^2$ we obtain $\sigma r^2 = 1/6\rho r^3 v_0^2$, where σ is the surface tension of the drop against air, r the initial drop radius, μ the viscosity of the surrounding fluid and $\nu = \mu/\rho$ the kinematic viscosity. Thus, the velocity v_0 initially transferred to the drop is $v_0 = \sqrt{6\sigma/\rho r}$. Once acquired,
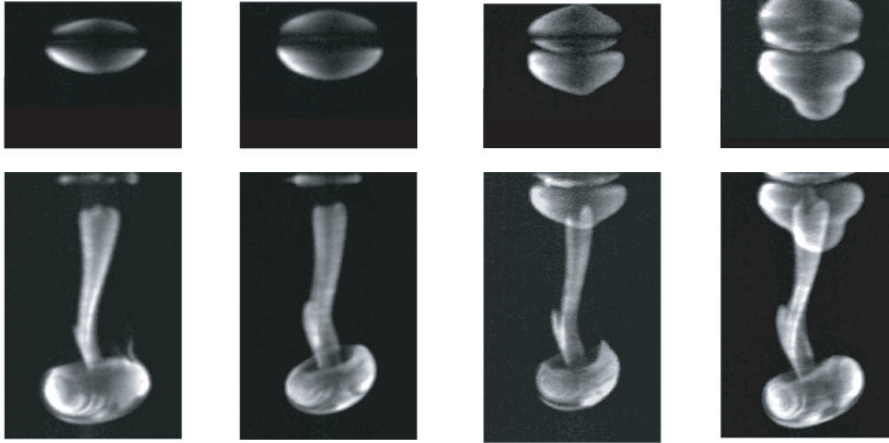
Fig. 2. Experimental side views of the drop injection. The fluid is water into water and the drop volume is $1\,\mu$l. Top: four initial stages of the drop injection. Bottom: four successive stages. Top and bottom images are separated by $20\,$ms whereas successive images on each raw occur after a fraction of ms [From [5]].

this velocity is dissipated by viscous processes that are accounted for by the Stokes law

$$\dot{v} = -\frac{\gamma\nu}{r^2}v, \tag{1}$$

where γ is a shape factor ($\gamma = 6\pi$ for a rigid sphere) [10]. Integrating the Stokes law yields

$$v(t) = v_0 e^{-\gamma\frac{\nu}{r^2}t} \tag{2}$$

and the maximum height h reached by the drop is

$$h = \int_0^\infty v(t)\,\mathrm{d}t = \frac{v_0 r^2}{\gamma\nu} = \frac{v_0}{\gamma}\tau_\nu \tag{3}$$

where $\tau_\nu = r^2/\nu$ is the viscous time scale. Substituting the expression for v_0 and considering that $r \propto V^{1/3}$, where V is the initial drop volume, h can be rewritten as

$$h = \frac{1}{\gamma}\sqrt{\frac{\sigma}{\rho\nu^2}}V^{1/2} \propto l_\nu^{-1/2}r^{3/2} \tag{4}$$

where we have included in γ all the geometric factors and we have defined the viscous length scale

$$l_\nu \equiv \frac{\rho\nu^2}{\sigma}. \tag{5}$$

In order to test the scaling law predicted predicted by the above dimensional arguments, we have performed several experiments by using mixtures of distilled water and Glycerol at different concentrations. For each fluid mixture and initial drop volume, we register on a videorecorder the entire process, from the drop injection until the ring stop and the onset of diffusion. The lateral and transverse images are combined through a video mixer so that we can follow on the same screen the vertical motion of the drop and the ring formation. By analyzing the video tapes, we can catch the images corresponding to the ring stop. On these images, we measure the vertical height h reached by the ring and its radius R (figure 3). R is measured as the average between the inner and the outer radius of the annulus.

3.1 Scaling laws

In figure 4 we report the measured height h as a function of the initial drop volume V for different fluid compositions, namely $0, 10, 20, 35$ and 52% of Glycerol in water. For each fluid
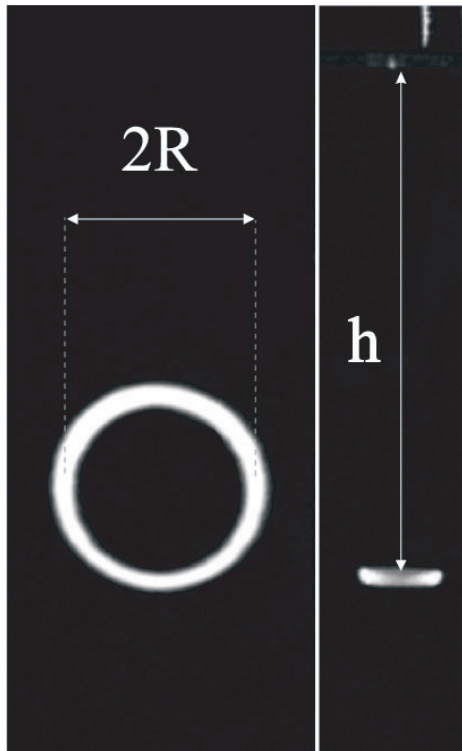
Fig. 3. Experimental images of the ring stop; left: transverse view, right: lateral view. [From [5]].
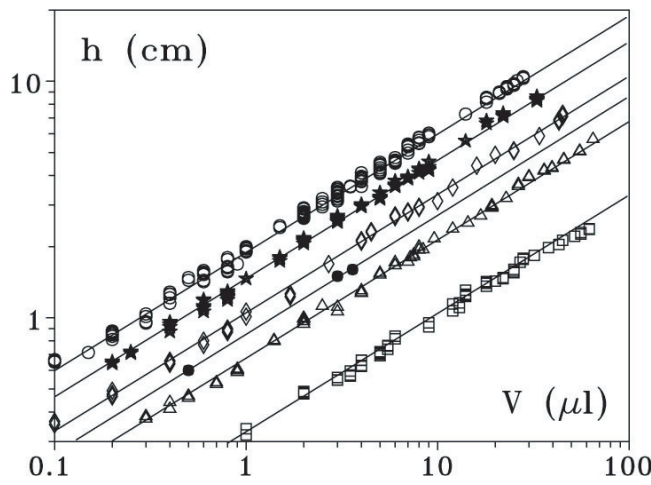
Fig. 4. h as a function of the initial drop volume V for different fluid compositions; empty circles: pure water, stars: 10% Glycerol in water (Gly), diamonds: 20% Gly, triangles: 35% Gly, squares: 52% Gly, filled circles: pure ethanol. [From [5]].

composition, $l_\nu = \sigma/\rho\nu$ is evaluated by substituting for σ, ρ and ν the values tabulated in the current literature [15]. By choosing a reference temperature of $20\,^\circ\text{C}$, which is the room temperature at which we perform the experiments, l_ν results to be equal to $72.4, 43.4, 24.9, 9.2, 2.2 \times 10^4\,\text{cm}^{-1}$ for, respectively, $0, 10, 20, 35, 52\%$ of Glycerol. The kinematic viscosity is, respectively, $\nu = 1.0, 1.3, 1.7, 2.7, 5.3 \times 10^{-2}\,\text{cm}^2\,\text{s}^{-1}$. The best fit lines are obtained by inserting into equation (4) the above values for the fluid parameters and by taking $\gamma = 15 \pm 1$ for the geometric factor. To have a further verification of the h versus V scaling law, we have performed an experiment by using ethanol as the fluid for the drop and the solvent. In this case, even though the viscosity is lower than for water, we expect that the ring stops at a smaller h because the surface tension has also been strongly reduced, thus reducing the initial speed transferred to the drop. The data
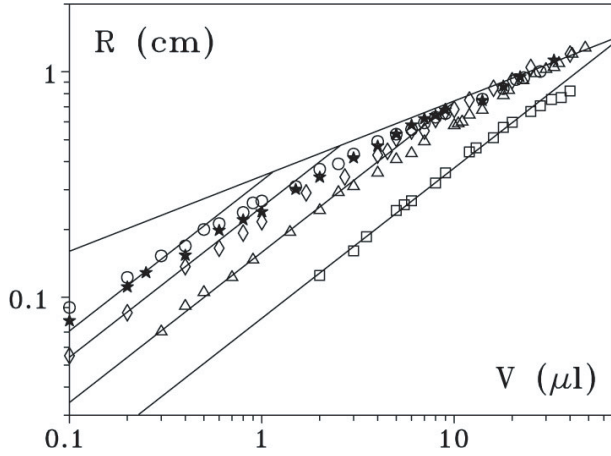
Fig. 5. R as a function of the initial drop volume V for different fluid compositions; empty circles: pure water, stars: 10% Gly, diamonds: 20% Gly, triangles: 35% Gly, squares: 52% Gly. Solid lines have two slopes, namely, 2/3 and 1/3. [From [5]].

do indeed scale as predicted by equation (4), once we set $l_\nu^{-1} = 12.5 \times 10^4 \, \mathrm{cm}^{-1}$, accordingly to the values tabulated for ethanol.

For the same sets of experiments, we report in figure 5 the measured radius R as a function of the initial drop volume V. Two distinct scaling regions can be observed, depending on the volume and viscosity. For small volumes and large viscosities the exponent of the power law fitting the data is close to 2/3 whereas for larger volumes and smaller viscosities data are fit by a 1/3 exponent. Moreover, in this latter case R seems not to depend on the fluid parameters but only on the initial drop volume. As it can be seen in figure 5, the 1/3 and 2/3 scalings correspond to two asymptotic behaviors, the separation between them depending on the fluid parameters. These two asymptotic behaviors can be explained by using dimensional arguments. The drop injection gives rise to a vortical motion of the fluid and the vortex ring transfers part of the initial velocity in the horizontal direction, thus giving rise to a transverse component of velocity, $v_\perp$. Once acquired, the horizontal velocity is dissipated by viscosity with a dissipation rate $1/\tau_\nu$. Therefore, the final ring radius should behave as $R \simeq v_\perp \tau_\nu = v_\perp r^2 \, \nu$. The initial acceleration of the vortical motion is given by $a = v_0^2/r$; therefore the radial velocity of the vortex built over a characteristic time τ_ν is given by $v_\perp \simeq a\tau_\nu = v_0^2 \tau_\nu/r$. It then results $v_\perp \simeq \sigma/\rho\nu$ and $R \simeq r^2/l_\nu = V^{2/3}/l_\nu$, which corresponds to the 2/3 scaling observed for small volumes and large viscosities. On the other hand, if the viscosity is small or the volume is large the rate of the vortex rotation is reduced. Indeed, in this case the boundary layer thickness $\delta = r(Re)^{-1/2} = r[\nu/(v_0 r)]^{1/2}$ shrinks and hence the transfer from the initial velocity v_0 to the effective vortical velocity v_{eff} implies a reduction factor δ/r, that is, $v_{\mathrm{eff}} = v_0\delta/r$. Hence $v_\perp = v_{eff}^2 \tau_\delta/r$ where $\tau_\delta = \delta^2/\nu$ is the viscous time along the length δ. It follows $v_\perp = \nu/r$, so that $R \simeq v_\perp \tau_\nu = r = V^{1/3}$. Thus, the $V^{1/3}$ law describes the region characterized by small viscosity and large volumes.

4 Positive density difference

4.1 The drop break-up

The break-up phenomena appear when there is a density difference $\Delta\rho$ between the drop and the solvent. In this case, Rayleigh–Taylor (RT) and Kelvin-Helmoltz (KH) instabilities are simultaneously present. However, we will see that, while KH remains dominant during the initial stages of the drop evolution, RT takes place later, when the ring is well developed. It is at this point that, because of the RT mechanism, initially small undulations start to be amplified leading to the fragmentation of the ring. The fragmentation process was first studied for $\Delta\rho > 0$, with different fluid parameters $\Delta\rho/\mu$ and different drop volumes V [6,7].

In a first set of experiments, to observe conveniently the initial stages of the process, the drop evolution is slowed down by playing on the quantity $\Delta\rho/\mu$. A drop of 90% Glycerol and 10%
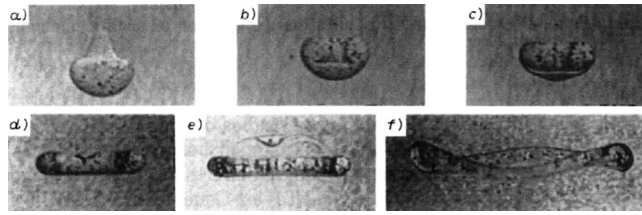
Fig. 6. Evolution of a falling drop with $r = 0.29\,\mathrm{cm}$ and $\Delta\rho = 0.0789\,\mathrm{g/cm^3}$. (a)–(f) Sequence of lateral views taken at the following positions from the free surface and times from the deposition: a) 2.0 cm, 1.05 s; b) 6.0 cm, 3.03 s; c) 8.0 cm, 4.0 s; d) 10.0 cm, 5.2 s; e) 13.0 cm, 7.34 s; f) 16.0 cm, 10.0 s. Panel e) shows the appearance of the turban instability and panel f) shows the onset of the R-T instability. [From [6]].

water with a volume of 1 μl and seeded with carbon particles (size $\sim 70\,\mu$m) is made to fall in solvent of 60% Glycerol and 40% water. The falling drop generates growing vorticity and shear at the interface between the two fluids. Thus, the drop transforms into a ring shape leaving behind a concave membrane attached to the torus to form a turban. This turban instability is evident in figure 6. We will see in the following that the turban instability takes place also in the case of $\Delta\rho > 0$, leaving behind the drop a convex, instead of a concave, membrane.

Then, the drop composition of 40% Glycerol, 60% water and the solvent composition of 25% Glycerol, 75% water were chosen and the drop volume was varied from 1 to 24 μl. Typical experimental pictures of bottom views of multiple fragments after the first break up are shown in figure 7. Experimental side views of successive multiple fragmentations are shown in figure 8. The cascade of fragmentations as seen in figure 8 stops after three steps, when the radius of the tertiary droplets has become so small that diffusion sets in and takes over the process. A bounded 2D version of the drop fragmentation was later explored in Pamplona by Carlos Perez and colleagues, uncovering an interesting phenomenology [14], especially confirming the vortical motion of the fluid during the first stages of the drop evolution.

4.2 Non-dimensional numbers

The drop break-up and its disappearance by diffusion are ruled by the non-dimensional number F. This is expressed as the ratio of the two characteristic times of the drop evolution. The falling drop behaves in such a way that the downward force due to gravity is proportional to the density difference $\Delta\rho$ between the two fluids. After a transient regime, an equilibration time $\tau' = \rho r^2/\mu$ (where ρ is the drop density, r the drop radius and μ the surrounding fluid viscosity) is reached, when the gravity force is compensated by the Stokes force, $F_s = -\gamma\mu r v$, with γ a shape factor ($\gamma = 6\pi$ for a rigid sphere). Thus, in the sedimentation regime, the asymptotic velocity $v_\infty = g\Delta\rho r^2/\gamma\mu$ is reached.

Therefore, the fragmentation of a drop falling with the asymptotic velocity implies the onset of a circular velocity, and this requires at least a time τ_1 corresponding to the transfer of v_∞ across the drop radius, that is, $\tau_1 = r/v_\infty \sim \mu/\Delta\rho g r$, where we have neglected the constant geometrical factor γ. Such a process is counteracted by diffusion, which takes place over the

|(a)|(b)|(c)|(d)|(e)|
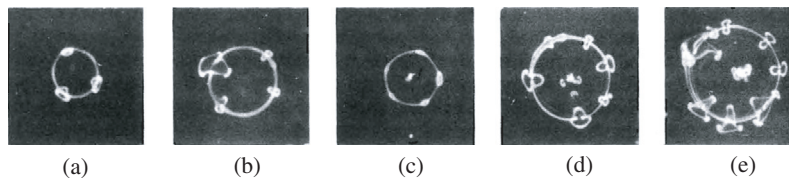
Fig. 7. Experimental snapshots showing examples of multiple fragments after the first break-up of the torus into: a) three, b) four, c) five, d) six, and e) seven fragments. [From [7]].
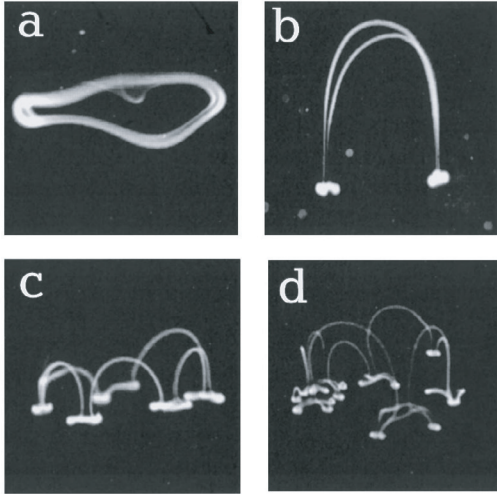
Fig. 8. Experimental side views of the drop falling in a lighter solvent; a) the drop, initially spherical, has become a torus; some regions with greater density give rise to successive fragmentations, b) two or c) six, depending on the fluid parameters. In d), the six secondary droplets of panel c) split again during the last stage of fragmentation. [From [8]].
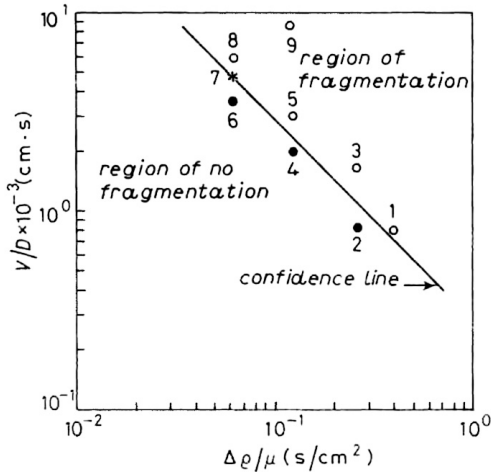
Fig. 9. Log-log plot of V/D versus $\Delta\rho/\mu$ for different nine experimental situations. The confidence line corresponds to $F_c = g(\Delta\rho V/\mu D)_c = (2.8\pm0.1)\times 10^5$. [From [6]].

time $\tau_2 = r^2/D$. The fragmentation then stops at a radius where τ_1 becomes longer than the diffusion time. The Fragmentation number F is thus defined as [6]

$$F = \frac{\tau_2}{\tau_1} = g\frac{\Delta\rho}{\mu}\frac{V}{D} \qquad (6)$$

and fragmentation takes place when F is greater than F_c, the critical Fragmentation number. When initial drops with $F > F_c$ undergo fragmentation, then the daughter drops may or not fragment again, depending if their volume is such that F is greater or smaller than F_c. Plotting V/D against $\Delta\rho/\mu$ as shown in figure 6, F_c was measured to be $(2.8 \pm 0.1) \times 10^5$, as derived from the boundary line distinguishing between the break-up and non break-up of the torus developing from drops with various fluid compositions [6].

F is found to be independent of the nature of the two miscible fluids. However, it was observed that within the τ_1 and τ_2 interval, there is a break up time τ_{bu} for the first fragmentation to take place [7]. Two forces, namely the gravity and the viscous drag, act on the spherical drop falling in a quiescent liquid. The net force is given by the sum of the buoyancy force, $F_b \propto \Delta\rho V g$, and the drag term due to the Stokes force, $F_s \propto \mu r v$. At large times the drop reaches the sedimentation velocity $v_\infty \propto \Delta\rho g r^2/\mu$. The third characteristic time of the process is the viscous time, $\tau_\nu = r^2/\nu = \rho r^2/\mu$. Depending on the fluid parameters, τ_ν can be larger or smaller of the first break-up time τ_{bu}, hence determining the extension of the fragmentation
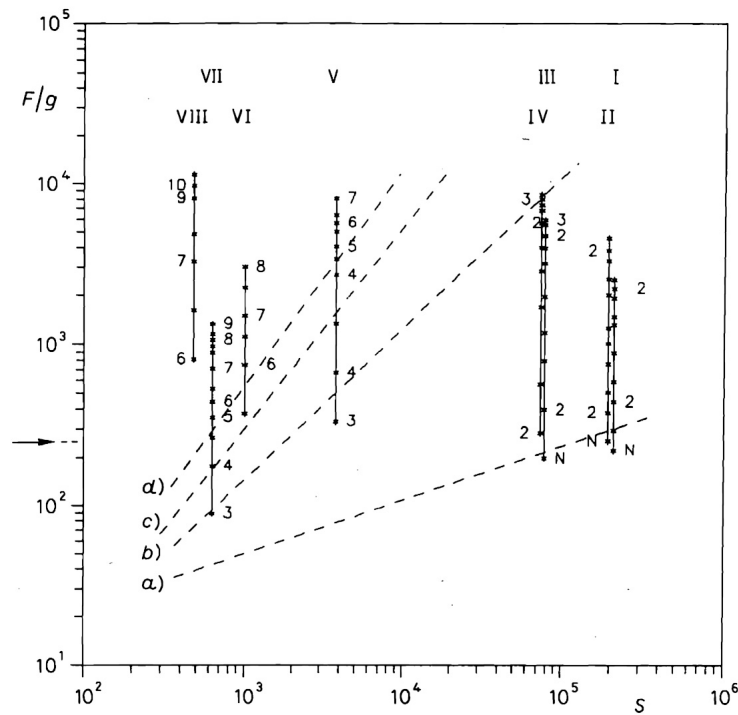
Fig. 10. $F - S$ diagram showing the number of fragments along the vertical line of F-axis. I to VIII refer to different fluid compositions [7]. The arrow denotes F_c/g. [From [7]].

regime. Indeed, if $\tau_1 = r/v_\infty$, which is the minimum time for the formation of the vortex ring, is much larger than τ_ν, then the ring disappears by diffusion, while for $\tau_\nu > \tau_1$ the torus has enough time to experience the local perturbations coming from the increasing velocity and thus becomes unstable. As a consequence, the ratio [7]

$$T = \frac{\tau_1}{\tau_\nu} = \frac{\mu^2}{g\rho\Delta\rho V} \tag{7}$$

accounts for an increasing number of fragments associated with the first break up when τ_ν is increased. By relating the diffusion time τ_2 to the viscous time τ_ν, the ratio

$$S = \frac{\tau_2}{\tau_\nu} = \frac{\mu}{\rho D} \tag{8}$$

can be defined as the second characteristic non dimensional number of the problem. This coincide with the Schmidt number, which depends only on the fluid properties [7]. One can control the fluid parameters in such a way that when τ_ν is increased and S decreased, then the number of the horizontal fragments would increase. A $F - S$ diagram showing the number of fragments obtained for different fluid compositions is displayed in figure 10.

5 Fractal properties of the fragmentation instability

In order to understand the self-similar process of the drop fragmentation, the same experimental set up as in figure 1 was used, but the solvent is illuminated horizontally with a collimated argon ion laser beam shaped as a thin lamina (500 μm thickness) by means of a cylindrical lens [8]. By changing the height of the lamina, the drops at different times and heights were followed. Beneath the cell is placed a plane mirror at an angle of $45°$, that reflects the fluorescence induced by the passage of the drop through the two-dimensional slice of light. The drop break up at
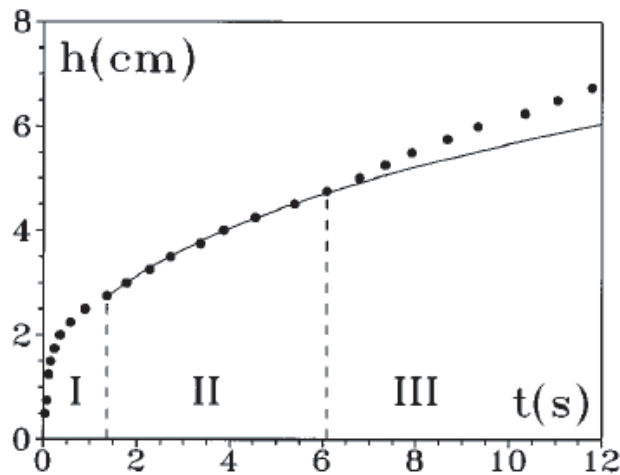
Fig. 11. Measured drop height as a function of the arrival time t, for an initial drop volume of $2\,\mu$l. The two vertical dashed lines mark the three regions identified as: I the first break-up region, ruled by the Fragmentation number F, II the fragmentation region, whose extension depends on the Schmidt number S, and III the region of pure diffusion. [From [8]].
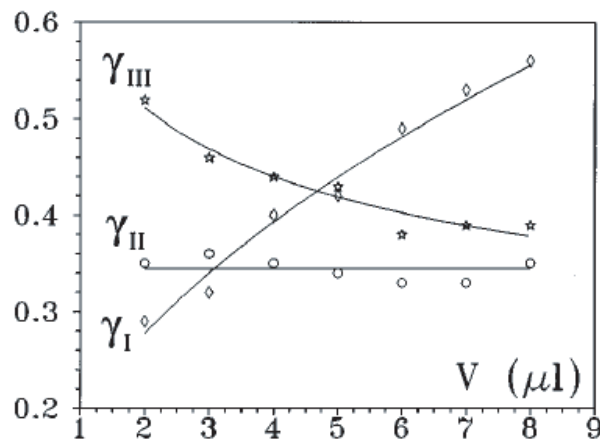
Fig. 12. Scaling exponents γ_I, γ_{II}, and γ_{III} of the height vs time $h \sim t^{\gamma}$ for the three different regions, respectively, as a function of the initial drop volume. The points are experimental data and the solid lines are best fits with $\gamma_I \sim V^{0.50\pm0.02}$ for the onset of the turban instability, $\gamma_{II} \sim V^{0.00\pm0.02}$ for the fragmentation region and $\gamma_{III} \sim V^{0.22\pm0.02}$ for the onset of diffusion. The second region shows a universal behaviour with an exponent $\gamma_{II} = 0.34 \pm 0.02$ independent from the initial drop volume. [From [8]].

different cell heights is ruled by the fluid parameters and the cell is large enough to exclude the influence of the lateral boundaries. Using different drop volumes, a series of sectional images ranging from 64×64 up to 320×320 pixels are recorded at ten different successive heights and times. Each digitized image contained levels of the normalized intensity varying from 0 to 255.

Using a drop of volume $2\,\mu$l, the height $h(t)$ versus time was plotted, as shown in figure 11. Three distinct regions can be distinguished, namely: region I indicates the initial drop fall, region II shows the fragmentation process and region III corresponds to the onset of diffusing droplets. For the three regions we formulate a power law as $h \sim t_i^{\gamma}$ with γ_i different exponents. By plotting the scaling exponents versus the drop volume as shown in figure 12, it can be deduced that $\gamma_i \sim V^x$ as follows: in region I, we have a relation of $\gamma_I \sim V^{0.50\pm0.02}$, in region II, $\gamma_{II} \sim V^{0.00\pm0.02}$
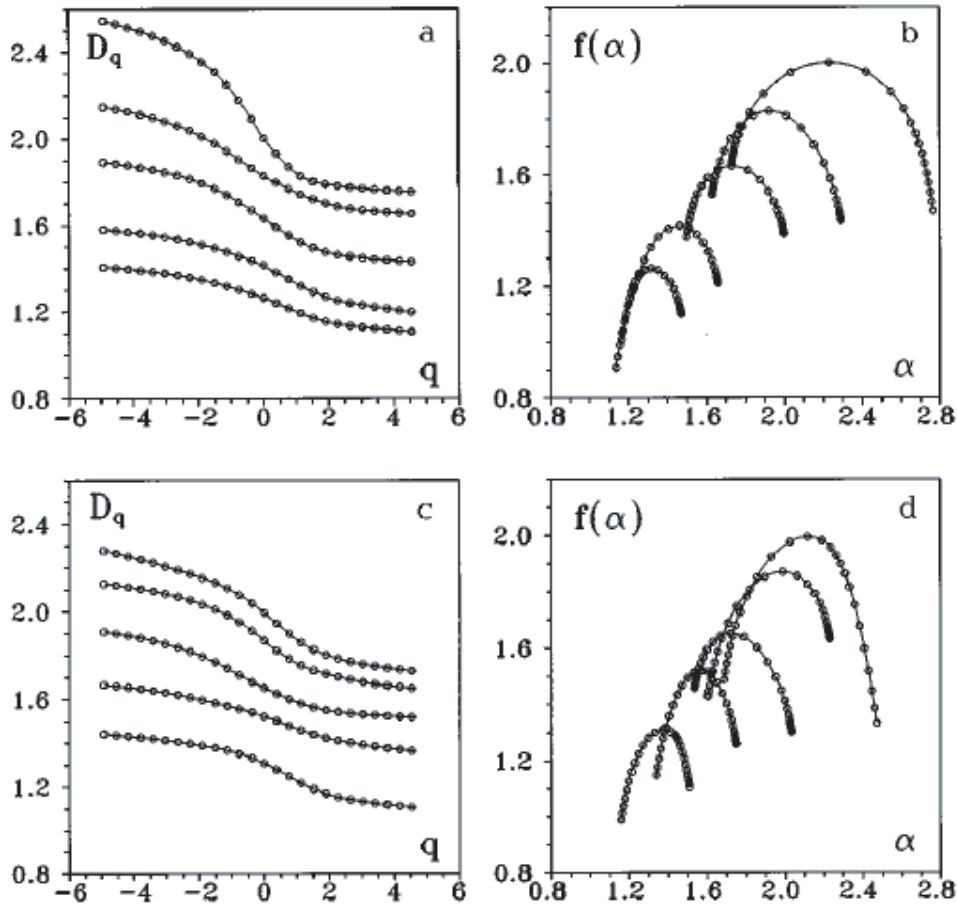
Fig. 13. Multifractal properties of the falling drop. Plots of a) D_q versus q and b) $f(\alpha)$ versus α for different heights, $h = 12, 22, 27, 32, 47$mm from top to bottom. Plots of c) D_q versus q and d) $f(\alpha)$ versus α for different heights, $h = 80, 110, 140, 170, 260$mm from bottom to top. The upper part, a) and b), shows the regime of increasing fractalization (instabilities prevailing over diffusion), the lower part, c) and d), shows the decreasing fractalization (diffusion overcoming instabilities). [From [8]].

while in region III, $\gamma_{III} \sim V^{0.22 \pm 0.02}$. The second region, which is the fragmentation region, shows a universal behaviour with an exponent $\gamma_{II} = 0.34 \pm 0.02$ independent from the initial drop volume.

Moreover, with the recorded digitized images and by using a box counting algorithm [17], we have computed the fractal dimension D_0 of the space occupied by the drop. The image space is partitioned into equally sized cubes of side ε. If $N(\varepsilon)$ is the number of cubes required to cover the space, the Renyi dimension can be calculated according to

$$D_q = lim_{\varepsilon \to 0} \frac{1}{q-1} \frac{\ln \sum_{i=1}^{N(\varepsilon)} p_i^q}{\lim \varepsilon} \tag{9}$$

where p_i is the image probability in the i-th box defined as follows: in the discrete frame processing, we split the $N \times N$ pixels frame into $m \times m$ pixels boxes, where m specifies the discrete ε value selected. If we call x, y the pixel coordinates, then the i-th box will span the coordinates from x_i to $x_i + m$ and y_i to $y_i + m$. Calling I_{xy} the intensity recorded at the pixel

(x, y), the total signal is given by

$$I_t = \sum_{x,y=1}^{N} I_{xy} \tag{10}$$

whereas the local signal in the i-th box is given by

$$I_i = \sum_{x=x_i}^{x_{i+m}} \sum_{y=y_i}^{y_{i+m}} I_{xy}. \tag{11}$$

With this in mind we define as the image probability of the i-th box the quantity

$$p_i = \frac{I_i}{I_t}. \tag{12}$$

According to equation (9), if log-log plots of $[\sum_{i=1}^{N(\varepsilon)} p_i^q]^{1/(q-1)}$ versus ε are plotted, the slopes of the linear regions correspond to D_q [18]. D_q curves can be derived for different drops at different heights (such as $h = 12, 22, 27, 32$ and $47\,\mathrm{mm}$) in the fractalisation region and for the region of diffusion ($h = 80, 110, 140, 170$ and $260\,\mathrm{mm}$) where fractalisation is decreasing. From the D_q curves, the $f(\alpha)$ curves were calculated by the Legendre transforms [19] with $d = 2$ for two-dimensional sections of the flow:

$$\alpha = \frac{\mathrm{d}}{\mathrm{d}q}[(q-1)D_q] + 1 - d \qquad f(\alpha) = q(\alpha - 1 + d) - (q-1)D_q. \tag{13}$$

The function $f(\alpha)$ describes how densely a singularity of strength α is distributed over the analyzed set. Thus, $f(\alpha)$ can also be seen as the fractal dimension of the subset over which the singularities scale as α. A set characterized by a spectrum of these dimensions is called multifractal since it can be thought of as constituted by many fractal subsets [20]. In figure 13 we report the $f(\alpha)$ versus α curves as it were done [8] for different height regions, h from 12 to $47\,\mathrm{mm}$ and h from 80 to $260\,\mathrm{mm}$, of the drop sections and for a drop volume of $4\,\mu\mathrm{l}$. From these curves, the fractal dimension D_0 of each image was deduced from the maximum of $f(\alpha)$ versus α plot.

A plot of the measured fractal dimension D_0 as a function of the cell height h is shown in figure 14. Here, it is observed that $D_0 = 2$ when the drop is whole up to torus, whereas at the onset of fractalisation D_0 reduces to 1.3. Once the fractalisation is over and inhibited by diffusion, a reverse process, leading to the restoration of the dimension $D_0 = 2$, takes place. This reverse process for height inside the cell, h from 80 to $260\,\mathrm{mm}$, is slow over a large range. Similar results are obtained for different drop volumes. Thus, the drop fragmentation is a transient fractal taking place before the establishment of pure mixing between drop and solvent. Inside the fractalisation region, the fragmentation cascade shows the generic properties of self-similar processes [8].

6 Negative density difference

We have studied the drop fragmentation instabilities in the case $\Delta\rho < 0$, that is, when the drop is lighter than the solvent [9]. Different fluid compositions were tested, namely the solvent was made up of distilled and purified water doped at 10, 15, 25% Glycerol and the drop was made up of distilled and purified water with a Glycerol concentration varying in between 0 and 25%. A typical behavior observed for a $V = 2\,\mu l$ drop doped at 15% Glycerol and falling in a 25% Glycerol doped solvent ($\Delta\rho = 0.053\,\mathrm{g/cm}^3$) is shown in figure 15. We can distinguish the fast injection of the drop, the ring formation, its undulation and the subsequent fragmentation into four droplets, then rising-up towards the free surface of the solvent. It is worth to note that, when the ring expands, it remains attached to a convex membrane. In the case of positive $\Delta\rho$ the same phenomenon was observed and called turban instability [6]. In that case the curvature
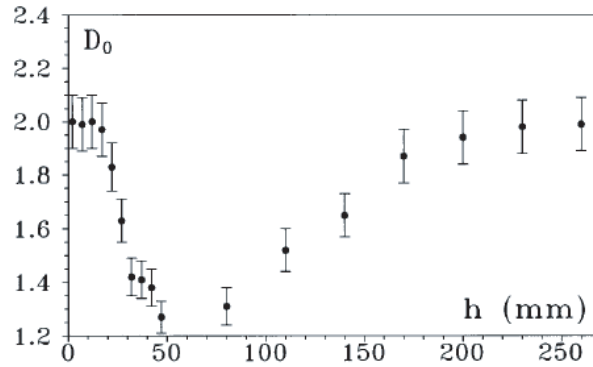
Fig. 14. Measured fractal dimension D_0 as a function of the cell height h. The initial drop, the torus and the final stages of diffusion have a dimension of 2. The dip of the curve corresponds to the fractalization region. [From [8]].

of the membrane was in the opposite direction with respect to the present case. Note that the turban instability has been observed also in the case of immiscible fluids [16].

We have performed several experiments by changing the drop volume V and the density difference $\Delta\rho$. For each set of experiments we have recorded several movies following the drop evolution and for each recorded movie we have performed the following processing. We have binarized all the frames by choosing a unique threshold intensity and by checking that this one minimizes the discontinuities between each frame and its successive. Then, on each frame we identify the center of mass of the drop, we record its coordinates and we follow its trajectory until the drop stops its descent and starts to rise up breaking into fragments. At this point, we choose only one fragment and follow its motion by recording the coordinates of its center of mass. The evolution of the longitudinal coordinate, h, of the center of mass is plotted as a function of time for a fixed drop volume, $V = 4\,\mu l$, and for different $\Delta\rho$ (figure 16) and for a fixed $\Delta\rho = 0.04505\,\mathrm{g/cm}^3$ and different drop volumes, $V = 2, 4, 6, 8\,\mu l$ (figure 17).

From figure 16 and 17, we can see that, once the drop has evolved into a vortex ring, it stops at a minimum height, h_{min}, which is mainly ruled by the initial drop volume, V. On the other hand, when fragmentation takes place, the rise-up time for the secondary droplets mainly depends on the density difference, $\Delta\rho$, eventually going to infinity for $\Delta\rho = 0$. At small $\Delta\rho$ the rise-up time is very long, while it shortens as $\Delta\rho$ increases. The drop injection takes place even in the absence of density difference because, the two fluids being miscible, there is an "instantaneous" conversion of the energy associated to surface tension into kinetic energy. Then, viscous dissipation slows down the motion of the drop, which asymptotically reaches the minimum height h_{min}.

To describe the dynamical behavior of the drop we have developed a simple model that takes into accounts buoyancy and viscous dissipation. The equation of motion reads

$$\frac{\mathrm{d}v}{\mathrm{d}t} = \frac{g\Delta\rho}{\rho} - \gamma\frac{\nu}{r^2}v, \tag{14}$$

with $r = \kappa\sqrt[3]{V}$ and γ, κ geometrical factors ($\gamma = 6\pi$ and $\kappa = 0.62$ for a rigid sphere [10]). The initial condition is given by the injection of the drop, $v(t = 0) = v_0$, where v_0 comes from the conversion of the drop surface tension into kinetic translational and rotational energy

$$\frac{1}{2}mv_0^2 + \frac{1}{2}I\omega^2 = 4\pi\sigma r^2, \tag{15}$$

with $I = \alpha mr^2$ the inertial momentum of the drop and $\omega = \beta v_0/r$ its frequency of rotation. If all the rotation is converted into translation, i.e., there is no sliding, then $\beta = 1$, otherwise
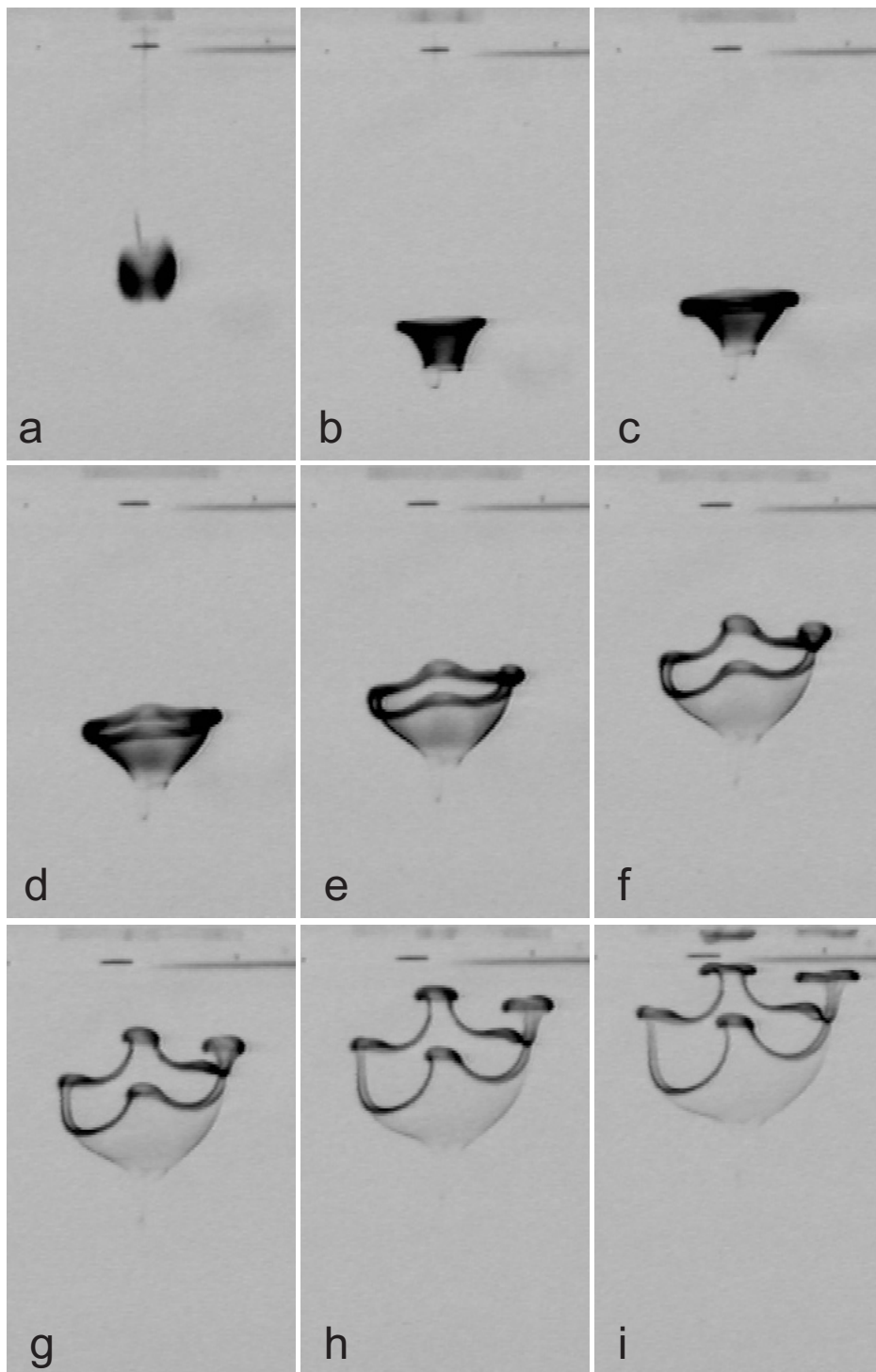
Fig. 15. Side views of the drop falling in a heavier solvent; a) the drop injection ($t = 0.08$ s), b) c) the ring formation ($t = 0.20, 0.32$ s), d) the development of the turban ($t = 0.44$ s), e) f) the onset of fragmentation ($t = 0.56, 0.68$ s), g) h) i) the rise up of the fragments ($t = 0.80, 0.92, 1.04$ s). [From [9]].
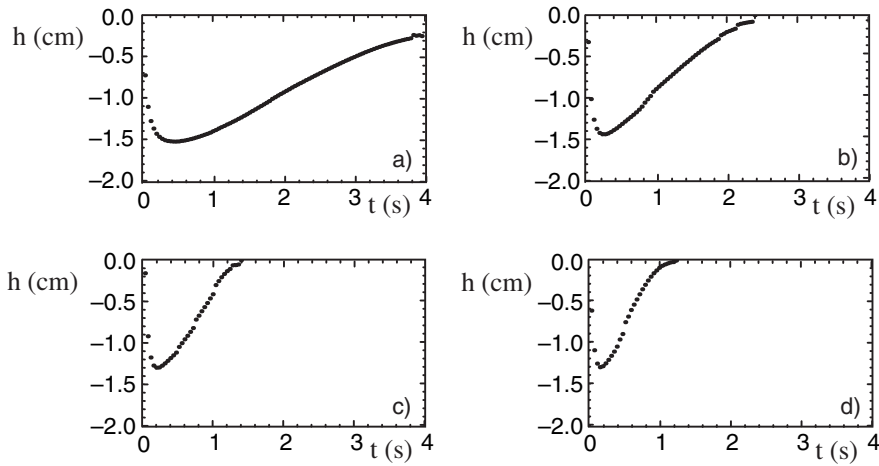
Fig. 16. Drop height h as a function of time for $V = 4\,\mu l$; $\Delta\rho =$ a) 0.01325, b) 0.0265, c) 0.03975 and d) 0.04505 g/cm^3.
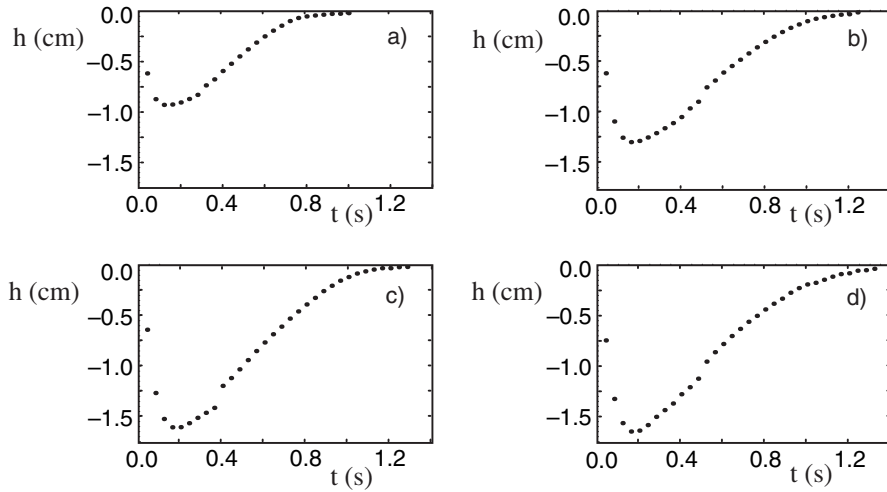
Fig. 17. Drop height h as a function of time for $\Delta\rho = 0.04505\,$g/cm^3; $V =$ a) 2, b) 4, c) 6 and d) 8 μl.

$\beta > 1$. We obtain for the initial velocity of the drop

$$v_0 = -\sqrt{\frac{6\sigma}{(1 + \alpha\beta^2)\rho r}}. \tag{16}$$

By defining the viscous time, $\tau_\nu = r^2/\gamma\nu$, we derive from equation (14) the drop asymptotic velocity, v_∞, corresponding to $dv/dt = 0$,

$$v_\infty = \frac{\Delta\rho}{\rho} g\tau_\nu = \frac{g\Delta\rho}{\mu} r^2, \tag{17}$$

which is the same expression previously derived for positive $\Delta\rho$. Integrating equation (14) from $v = v_0$ to $v = 0$ we obtain the drop fall-down time, τ_d, which is the time taken by the drop to stop

$$\tau_d = \tau_\nu \ln\left(1 - \frac{v_0}{v_\infty}\right), \tag{18}$$
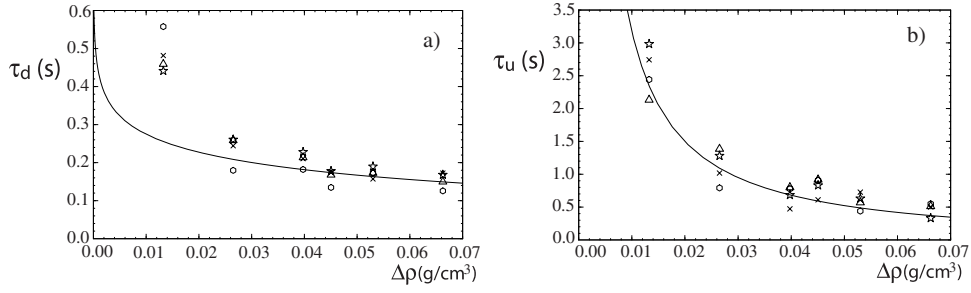
Fig. 18. a) Drop fall-down time τ_d and b) rise-up time τ_u as a function of $\Delta\rho$; $V = 2\,\mu l$ circles, $V = 4\,\mu l$ triangles, $V = 6\,\mu l$ stars, $V = 8\,\mu l$ crosses. Lines are the theoretical curves for $V = 5\,\mu l$.

and the minimum height, h_{min}, reached by the drop before rising-up

$$h_{min} = v_\infty \tau_d + v_0 \tau_\nu. \tag{19}$$

As for the fragment rise-up time τ_u, if $t \gg \tau_\nu$ it is simply given by

$$\tau_u = -\frac{h_{min}}{v_\infty} = \left|\frac{v_0}{v_\infty}\right|\tau_\nu - \tau_d, \tag{20}$$

so that the total elapsed time is $\tau_T = |v_0/v_\infty|\tau_\nu$. However, as we can see from figure 15, the rising-up droplets are fragments of the initial drop, so that the asymptotic velocity to be used here has the same expression as before, equation (17), but with a volume V/N that is a fraction of the initial one, where N is the number of fragments. If we take into account this correction, we have that

$$\tau_u = (\tau_T - \tau_d)N^{2/3}. \tag{21}$$

We show in figure 18(a) and figure 18(b) the drop fall-down time τ_d, and, respectively, the rise-up time τ_u, as a function of $\Delta\rho$. From now on, we fix the parameters of the model to $\alpha\beta^2 = 4$, $\gamma = 6.67$ and $\kappa = 0.56$. We plot in figure 18(a) the theoretical prediction for τ_d, as in equation (18). This curve fits quite well the data for $\Delta\rho > 0.02\mathrm{g/cm}^3$ but presents large deviations for lower values of $\Delta\rho$. Indeed, when $\Delta\rho \to 0$ the logarithmic divergence does not take into account the dissipation due to the increasing radius of the vortex ring. To include such an effect a more refined model should be developed in order to describe the dynamics of the ring formation. As for the rise-up time τ_u, we have plotted in figure 18(b) the experimental data by normalizing each value at $N^{2/3}$. By using the expression in equation (20), we obtain a good fit of all the data. In figure 18(b) we report the curve for $V = 5\mu l$, the curves for the other volumes being close to this one.

The minimum height h_{min} reached by the drop before rising-up is plotted in figure 19 as a function of $\Delta\rho$, together with the theoretical curves, equation (19), for $V = 2, 4, 6, 8\,\mu l$. We can see that the theoretical curves are in good agreement with the experimental data. Note that, in the limit of the experimental error, for $\Delta\rho = 0$ we obtain the $h \propto V^{\frac{1}{2}}$ scaling, in agreement with the previously reported law [5].

Finally, we rescale all the $h - t$ data by h_{min} and τ_T, and we plot the reduced profiles $h(t)$ in figure 20. We can see that all the drops approximately follow the same evolution law. The early stages of the drop injection are very similar to those observed at $\Delta\rho = 0$: the drop falls very fast inside the solvent and develops a ring. Then, the ring stops because of dissipation of the initial impulse. At this point, the drop has reached the minimum height h_{min}, where a velocity reversal occurs and where a new instability takes place leading to the fragmentation of the ring into smaller droplets. Being $\Delta\rho < 0$, the secondary droplets rise-up towards the surface because of buoyancy. This dynamical regime corresponds to the linear portions of the $h - t$ profiles just after h_{min}. Viscous dissipation slows down the motion of the fragments, but in this dynamical regime buoyancy is dominant.
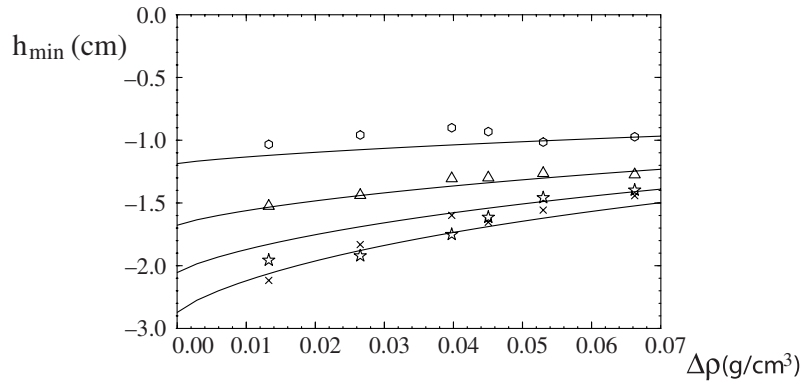
Fig. 19. Minimum drop height h_{min} as a function of $\Delta\rho$; $V = 2\,\mu l$ circles, $V = 4\,\mu l$ triangles, $V = 6\,\mu l$ stars, $V = 8\,\mu l$ crosses.
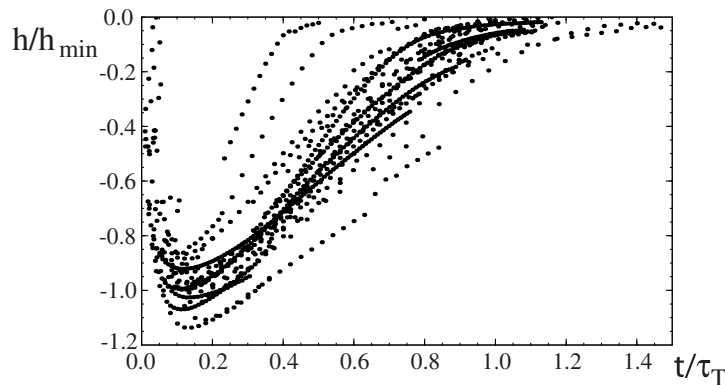
Fig. 20. Reduced $h - t$ profiles for the all the experiments in 25% Gly doped solvent.

At later times, when fragments approach the surface, we observe deviations from the linear dependence of $h(t)$. Indeed, droplets feel the presence of the boundary and behave as secondary vortex rings, each one colliding over a wall with a longitudinal velocity component [21]. To describe the interaction of the vortex ring with the wall we can replace the wall by the specular image of the vortex ring, this one having opposite circulation with respect to the incoming ring. Because of this interaction, the vortex ring expands and slows down, until, at later times, diffusion takes over the whole process.

7 Conclusions

In summary, the physics of liquid drops needs to be unveiled in order to have more relevant practical applications in agriculture and industry [22]. The experimental characterisation of the dynamical and statistical features of a drop falling in a miscible fluid can serve this purpose. The process can be associated with three dynamical regions, one corresponding to the onset of the torus and the first hydrodynamic instabilities, the other characterised by the successive fragmentation of the initial drop into smaller droplets and the last one dominated by diffusion, in which the droplets mix with the solvent without undergoing further fragmentations. The drop dynamics is ruled by three characteristic times through which two non-dimensional numbers, namely the Fragmentation number F and the Schmidt number S, were derived. While the first region of the drop becoming a torus is ruled by F, the fragmentation region of successive break-up is determined by S. In order to understand the development of the torus at the early stages of the drop before rupture, further experiments were performed on the role of the interfacial tension

and its dissipation energy. The initial stage of the drop injection was found to be independent of the density difference between the drop and the solvent being either positive or negative. In the fragmentation region, the fractalization can be attributed to a multifractal structure of the droplet projections at different height. By using scaling laws on the drop volume V and various height h reached before the formation of the torus and also during the fragmentation process, h and V can be rescaled to universal power law behaviours.

References

1. J.J. Thomson, H.F. Newall, Proc. Royal Soc. **39**, 447 (1885)
2. D.W. Thomson, *On Growth and Form* (Cambridge University Press, 1963)
3. N. Baumann, D.D.J. Joseph, P. Mohr, Y. Renardy, Phys. Fluids A **4**, 567 (1992)
4. D.J. Korteweg, Arch. Neerl. Sci. Ex. Nat. II **6**, 1 (1901)
5. S. Residori, E. Pampaloni, P.K. Buah-Bassuah, F.T. Arecchi, Eur. Phys. J. B **15**, 331 (2000)
6. F.T. Arecchi, P.K. Buah-Bassuah, F. Francini, C. Perez-Garcia, F. Quercioli, Europhys. Lett. **9**, 333 (1989)
7. F.T. Arecchi, P.K. Buah-Bassuah, C. Perez-Garcia, Europhys. Lett. **15**, 429 (1991)
8. F.T. Arecchi, P.K. Buah-Bassuah, F. Francini, S. Residori, Phys. Rev. E **54**, 424 (1996)
9. P.K. Buah-Bassuah, R. Rojas, S. Residori, F.T. Arecchi, Phys. Rev. E **72**, 067301 (2005)
10. D.J. Tritton, *Physical Fluid Dynamics* (Oxford University Press, New York, 1988)
11. See e.g. D.D. Joseph, Eur. J. Mech. B/Fluids **9**, 565 (1990); P. Petitjeans, T. Maxworthy, J. Fluid. Mech. **326**, 37 (1996); E. Lajeunesse, J. Martin, N. Rakotomalala, D. Salin, Phys. Rev. Lett. **79**, 5254 (1997)
12. S. Middleman, *Modeling Axisymmetric Flows* (Academic Press, San Diego, California, 1995)
13. G.H. Ristow, Phys. Rev. E **55**, 2808 (1997)
14. A. Garcimartin, H.L. Mancini, C. Perez-Garcia, Europhys. Lett. **19**, 171 (1992)
15. R.C. Weast, *Handbook of Chemistry and Physics* (The Chemical Rubber Co., Cleveland, Ohio, 1971)
16. O.N. Boratav, R.B. Pelz, N.J. Zabusky, Phys. Fluids A **4**, 581 (1992)
17. H. Froechling, J.P. Crutchfield, D. Farmer, N.H. Packard, R. Shaw, Physica D **3**, 605 (1981)
18. R.R. Prasad, C. Meneveau, K.R. Sreenivasan, Phys. Rev. Lett. **61**, 76 (1988)
19. T.C. Hasley, M.H. Jensen, L.P. Kadanoff, I. Procaccia, B.I. Shraiman, Phy. Rev. A **33**, 1141 (1986)
20. J. Feder, *Fractals* (Plenum, New York, 1988)
21. E. Guyon, J.-P. Hulin, L. Petit, *Hydrodynamique Physique* (InterÉditions, Éditions du CNRS, Paris 1991), p. 323
22. See e.g. J. Eggers, Rev. Mod. Phys. **69**, 865 (1997)